EMISSION-LINE GALAXIES FROM THE *HUBBLE SPACE TELESCOPE* PROBING EVOLUTION AND REIONIZATION SPECTROSCOPICALLY (PEARS) GRISM SURVEY. I. THE SOUTH FIELDS

AMBER N. STRAUGHN[1], NORBERT PIRZKAL[2], GERHARDT R. MEURER[3], SETH H. COHEN[4], ROGIER A. WINDHORST[4],
SANGEETA MALHOTRA[4], JAMES RHOADS[4], JONATHAN P. GARDNER[1], NIMISH P. HATHI[5], ROLF A. JANSEN[4], NORMAN GROGIN[2],
NINO PANAGIA[2], SPERELLO DI SEREGO ALIGHIERI[6], CARYL GRONWALL[7], JEREMY WALSH[8], ANNA PASQUALI[9], AND CHUN XU[10]

[1] Astrophysics Science Division, Observational Cosmology Laboratory, Goddard Space Flight Center, Code 665, Greenbelt, MD 20771, USA;
Amber.N.Straughn@nasa.gov
[2] Space Telescope Science Institute, Baltimore, MD 21218, USA
[3] Department of Physics and Astronomy, Johns Hopkins University, Baltimore, MD 21218, USA
[4] School of Earth and Space Exploration, Arizona State University, Tempe, AZ 85287, USA
[5] Department of Physics & Astronomy, University of California, Riverside, CA 92521, USA
[6] INAF-Osservatorio Astrofisico di Arcetri, I-50125 Firenze, Italy
[7] Department of Astronomy & Astrophysics, Pennsylvania State University, University Park, PA 16802, USA
[8] ESO Space Telescope European Co-ordinating Facility, D-85748 Garching bei München, Germany
[9] Max-Planck-Institut for Astronomie, Koenigstuhl 17, D-69117 Heidelberg, Germany
[10] Shanghai Institute of Technical Physics, 200083 Shanghai, China

ABSTRACT

We present results of a search for emission-line galaxies (ELGs) in the southern fields of the *Hubble Space Telescope* Probing Evolution And Reionization Spectroscopically (PEARS) grism survey. The PEARS South Fields consist of five Advanced Camera for Surveys pointings (including the Hubble Ultra Deep Field) with the G800L grism for a total of 120 orbits, revealing thousands of faint object spectra in the GOODS-South region of the sky. ELGs are one subset of objects that are prevalent among the grism spectra. Using a two-dimensional detection and extraction procedure, we find 320 emission lines originating from 226 galaxy "knots" within 192 individual galaxies. Line identification results in 118 new grism-spectroscopic redshifts for galaxies in the GOODS-South Field. We measure emission-line fluxes using standard Gaussian fitting techniques. At the resolution of the grism data, the Hβ and [O III] doublet are blended. However, by fitting two Gaussian components to the Hβ and [O III] features, we find that many of the PEARS ELGs have high [O III]/Hβ ratios compared to other galaxy samples of comparable luminosities. The star formation rates of the ELGs are presented, as well as a sample of distinct giant star-forming regions at $z \sim 0.1$–0.5 across individual galaxies. We find that the radial distances of these H II regions in general reside near the galaxies' optical continuum half-light radii, similar to those of giant H II regions in local galaxies.

Key words: catalogs – galaxies: starburst – techniques: spectroscopic

Online-only material: color figures, machine-readable and VO tables

1. INTRODUCTION

The Probing Evolution And Reionization Spectroscopically (PEARS[11]) Advanced Camera for Surveys (ACS) grism survey provides a 200 *Hubble Space Telescope* (*HST*) orbit data set from which one can investigate many different aspects of galaxy evolution. High-redshift objects such as Lyα galaxies, Lyman break galaxies (LBGs), and active galactic nuclei (AGNs) are being investigated by Rhoads et al. (2009) and N. Grogin et al. (2009, in preparation). Elliptical galaxies (Ferreras et al. 2009), and emission-line galaxies (ELGs; Straughn et al. 2008) are also being studied. A similar deep grism program was carried out in the GRism ACS Program for Extragalactic Science (GRAPES) project (Pirzkal et al. 2004; Xu et al. 2007). Here we discuss results of a search for ELGs in the PEARS South Fields. In particular, we present new grism spectroscopic redshifts for 118 galaxies in the GOODS South Field, as well as discuss the ELG line luminosities, star formation rates (SFRs), and AGN candidates among the sample.

For many years, galaxies that are actively forming stars have been regarded as important objects for study in the context of galaxy assembly. In particular, the Hα, [O III], and [O II] lines

have been used extensively to determine their SFRs (Kennicutt 1983; Gallego et al. 1995; Gallego et al. 2002; Brinchmann et al. 2004; Westra & Jones 2008; Kewley et al. 2004; Glazebrook et al. 2004). Many projects have specifically used slitless spectroscopy in order to study ELGs. Ground-based slitless spectroscopy has been used by Kurk et al. (2004) to identify ELGs. Yan et al. (1999) derived the Hα luminosity function and SFR for galaxies at $z \gtrsim 1$ using the *HST* NICMOS G141L grism from the NICMOS Grism Parallel Survey (McCarthy et al. 1999). Teplitz et al. (2003) studied ELGs using the STIS Parallel Survey (Gardner et al. 1998) and Drozdovsky et al. (2005) presented ELGs from the *HST* ACS Grism Parallel Survey. Shim et al. (2009) have studied the luminosity function and evolution of the SFR density for ELGs using Hα, also using the NICMOS data. GRAPES (Pirzkal et al. 2004; Malhotra et al. 2005) has also yielded slitless spectroscopy for galaxies in the Hubble Ultra Deep Field (HUDF), including a large sample of ELGs (Pirzkal et al. 2006; Xu et al. 2007). PEARS is a follow-up grism survey to GRAPES, and provides a larger spectroscopic data set of ELGs in an eight times larger area. In Straughn et al. (2008), we investigated in detail several methods aimed at detecting these ELGs in the PEARS HUDF pointing. In the current paper, we use the most efficient method and extend that study to include the remaining four PEARS South ACS Fields. In Section 2, we

---

[11] http://archive.stsci.edu/prepds/pears.

discuss the PEARS data set used here. Section 3 outlines the methods used to detect the ELGs. In Section 4, we present results of the search, including a table of the South Field ELGs detected along with new spectroscopic redshifts, and a discussion of line luminosities, SFRs, AGN candidates, and the radial distribution of galaxy knots. In Section 5, we summarize our findings and discuss future prospects.

2. DATA

The *HST* PEARS grism survey consists of nine ACS Fields observed with the G800L grism. The G800L grism yields low-resolution ($R \sim 100$) optical spectroscopy between $\lambda = 6000$–9500 Å. Five fields were observed in the GOODS South region (including the HUDF) and four in GOODS North. Here we present properties of ELGs detected in the PEARS South fields. The PEARS HUDF was observed for 40 orbits (four roll angles, obtaining spectra for sources with limiting continuum AB magnitude $i'_{AB} \lesssim 27.0$ mag). The other four South PEARS fields were observed for 20 orbits each (three roll angles per field with spectra for sources with limiting continuum AB magnitude $i'_{AB} \lesssim 26.0$ mag). Limiting continuum magnitudes are estimated from the net spectral significance, which is a measure of the peak integrated signal-to-noise ratio (S/N) of a stacked spectrum, and is described fully for the GRAPES project in Pirzkal et al. (2004; see also S. Cohen et al. 2009, in preparation). Observations at multiple roll angles were made in each field in order to reduce the contamination from overlapping spectra in crowded regions. These multiple roll angles are also used in detecting viable emission-line sources, as described in the following section. S. Malhotra et al. (2009, in preparation) will describe the PEARS ACS grism observations in detail. Pirzkal et al. (2004) give a detailed description of the closely related prior GRAPES project. The PEARS North Fields are currently being reduced and a future paper presenting ELGs from the North Fields will be Paper II in this series of PEARS ELGs studies.

3. METHODS

We briefly outline the procedures used to detect ELGs in the PEARS grism data, using a two-dimensional detection method that takes advantage of the observation that emission lines typically originate from clumpy knots of star formation within galaxies. A detailed description of this method and comparison with several other extraction methods are given in Straughn et al. (2008).

3.1. Data Pre-Processing

The first step in the grism data reduction involves pre-processing of the grism data. Each grism image is median filtered and smoothed using a 13×3 smoothing kernel along the direction of the dispersion axis (i.e., unsharp-masked). We refer to Meurer et al. (2007) for a full description of this method of pre-processing ACS grism data in general. The dimension of smoothing kernal used does not greatly affect the sources that are selected. The choice of 13×3 smoothing kernel ensures efficient detection of real emission-line objects while largely avoiding faint image defects or other contaminants to the sample. This unsharp-masking step is performed in order to largely remove the continuum flux from the dispersed image, leaving behind sharp emission-line features. Zero-order images of compact sources are excluded in the triangulation step, described in the next section. Residual image defects are also retained, but are unique to each roll angle and are thus excluded in the
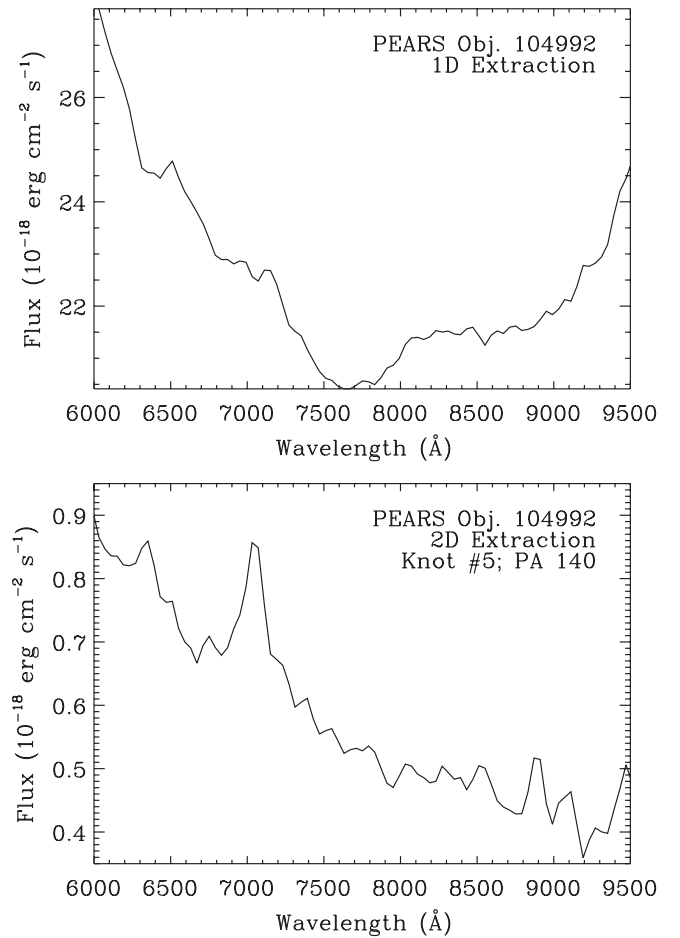
Figure 1. Advantage of the two-dimensional-detection method outlined in this paper (and described in detail in Straughn et al. 2008) for PEARS Object 104992. The top panel shows that continuum flux overwhelms the line when the spectrum of the entire galaxy is extracted (as would be the case in one-dimensional methods; see, e.g., Xu et al. 2007). However, the emission line at (observed-frame) 7000 Å is clearly seen when extraction of an individual knot is performed (bottom panel). See Figure 12 for an image of this object.

next steps as described below. In doing this, we isolate the actual emission line which would ordinarily be washed out by the continuum, and therefore missed in more traditional one-dimensional detection methods (see Figure 1). After the images are pre-processed in this manner, they are cataloged with the source extraction algorithm SExtractor (Bertin & Arnouts 1996), giving a list of compact sources. An average of 820 compact sources is initially selected from each field in this manner.

3.2. Emission Line Detection by Triangulation

The basis of this method of two-dimensional emission-line detection and wavelength calibration relies on each source being observed in more than one roll angle. The emitting source is traced back along the dispersion direction for each roll angle, and intersections of these traces are used to obtain the real sky coordinates (R.A., decl.), as well as the wavelength solution for that emitting source (see also Figure 2 of Straughn et al. 2008). In this way, image defects are excluded from the selection, since they would not ordinarily appear at the same physical location on the grism images and map onto a "source" as described here. This procedure is applied to all roll angle pairs, such that each source— that has three position angles observed, for example—has

Table 1
Global Properties of Emission-Line Galaxies

PEARS ID	Knot No.	R.A. (deg)	Decl. (deg)	i'_{AB} (mag)	Wavelength (Å)	Flux (10^{-18} erg s^{-1} cm^{-2})	EW (Å)	Line ID	Grism Redshift	Flag (*)
9359	1	53.1682091	−27.9300213	22.97	7349	21.2 ± 3.5	94	Hα	0.120	2
9359	2	53.1682892	−27.9300632	22.97	7385	19.7 ± 3.5	75	Hα	0.125	2
12250	1	53.1566811	−27.9257526	24.72	6671	57.0 ± 2.0	313	[O III]	0.337	1
12250	1	53.1566811	−27.9257526	24.72	8774	26.1 ± 5.3	199	Hα	0.337	1
12665	1	53.1541176	−27.9234123	22.06	7413	137.1 ± 6.4	214	⋯	⋯	⋯
13541	1	53.1584473	−27.9188538	21.49	6842	112.4 ± 2.8	111	[O III]	0.370	1
13541	1	53.1584473	−27.9188538	21.49	9059	75.7 ± 8.8	83	Hα	0.370	1
13541	2	53.1584740	−27.9189358	21.49	6802	16.5 ± 1.4	10	[O III]	0.370	1
13541	2	53.1584740	−27.9189358	21.49	9013	95.6 ± 11.2	76	Hα	0.370	1
13553	1	53.1643639	−27.9186115	19.46	7416	23.0 ± 6.9	19	Hα	0.130	2

Notes. * No data indicate that measurement was not possible. In the case of line IDs, no data indicate that no suitable line ID was found for the given input redshift. "Grism Redshift" column gives re-calculated redshift based on the line identification. "Flag" column gives source of input redshift used for line identification, if needed: 1, two lines visible in spectrum, no prior redshift needed; 2, single line in spectrum, line ID and grism redshift based on prior spectroscopic redshift; 3, single line in spectrum, line ID, and grism redshift based on prior photometric redshift; 4, single line in spectrum, line ID and grism redshift based on prior spectrophotometric redshift (see Section 3.3). Objects 68739–96627 are from the HUDF.
† CDF-S X-ray sources. From N. Grogin et al. (2009, in preparation) matches to PEARS sources.
‡ CDF-S X-ray sources with $L_X \gtrsim 10^{42}$ erg s^{-1} and thus likely AGNs. From N. Grogin et al. (2009, in preparation).
(This table is available in its entirety in machine-readable and Virtual Observatory (VO) forms in the online journal. A portion is shown here for guidance regarding its form and content.)

three calculations made (i.e., PA1-PA2, PA1-PA3, PA2-PA3). The HUDF, which has four position angles observed, thus has six calculations per source. This procedure produces the master catalog of ELG sources, which are then visually checked. In this visual confirmation step, there are occasional instances where an emission-line candidate was present in all three roll angles, and thus was included in the master catalog, but is not a genuine emission line. Such is the case for some bright galaxies that have continuum "bumps" that appear in the grism image as compact sources: i.e., false line candidates. When examining the collapsed one-dimensional spectra from the individual sources, it is clear which sources are genuine emission lines and which are not. The genuine lines are subsequently retained for each field and the final wavelength for each line listed in Table 1 is obtained by averaging the results from the roll angle pairs described here. Here we define our terminology, since extractions were performed on individual galaxy "knots": a galaxy can have several knots, and each knot can have more than one line as allowed by the grism bandpass. An average of 90 knot candidates per field is retained in the automated triangulation step, and an average of 46 genuine knots per field is retained after the visual confirmation step. This method produced a total of 320 emission lines originating from 226 galaxy knots, within 192 individual galaxies in the five total PEARS South Fields (see Table 2).

3.3. Redshifts of Emission-Line Galaxies

For ELG knots that have only one emission line in their spectra—which is the case for 68% of the galaxy knots—a first-guess redshift is essential for line identification. For this we use the spectroscopic and photometric redshifts from the GOODS–MUSIC catalog (Grazian et al. 2006, and references therein). About 33% of the ELGs detected in the PEARS South Fields have spectroscopic redshifts and 85% have photometric redshifts. There is almost complete overlap between the two catalogs—less than 3% of sources have spectroscopic redshifts but no photometric redshifts. Where no spectroscopic or photometric redshift exists for a particular source, we match our sources against the table of spectrophotometric redshifts of

S. Cohen et al. (2009, in preparation)—which are determined by using a combination of both the grism spectra and broadband data (see also Cohen et al. 2009; Ryan et al. 2007). Spectra with strong lines, however, are often assigned artificially high spectrophotometric redshifts due to the presence of such lines that are absent from the template spectral energy distributions (SEDs) used. In total, there were 16 galaxies that had only a spectrophotometric redshift, five of which had two lines in the observed wavelength interval and therefore had a grism redshift calculated based on the line ratio. Of the galaxies with a single line in the spectrum and only a spectrophotometric redshift, three had spectrophotometric redshifts in concordance with the observed line and were used to deduce final identification. For 31 objects with a single line where either no prior redshifts were available, or the spectrophotometric redshifts do not agree with any of the likely line identifications, no redshift was assigned.

Line identification proceeds as follows. For galaxy knots that have both Hα/[O III], [O III]/[O II], or C III]/C IV in the observed wavelength range, the ratio of the observed line wavelengths is computed to obtain a direct line identification and redshift—without need of a first-guess redshift. For galaxy knots with only a single line, the existing spectroscopic, photometric, or spectrophotometric redshifts (in order of preference) from Grazian et al. (2006) and S. Cohen et al. (2009, in preparation) are used to determine the most likely identification of the single line within the redshift and intrinsic grism errors. Redshifts based on these identifications and measured line positions are subsequently recalculated and given in Table 1.

Line fluxes are derived using standard Gaussian fitting techniques and measured lines with S/N $\gtrsim 2$ are retained in the final catalog (Figure 6). 96% of objects have S/N $\gtrsim 3$. Since the [O III] line—which is usually the strongest of the lines we detect—is blended with Hβ due to the grism spectral resolution, we fit two Gaussian components. In these two-component fits, the central wavelengths of the [O III] and Hβ lines are constrained to have the correct wavelength ratio. In order to reduce the number of free parameters that go into the fits of the low-resolution grism spectra, we examine individually a subsample of 15 representative test case spectra, varying the ratio of

Table 2
Summary of ELG Detections in South Fields

Field	No. of Lines	No. of Knots	No. of Galaxies	No. of Galaxies with Multiple Knots	No. of Knots with Multiple Lines
HUDF	98	78	64	12	15
South 1	51	37	35	2	8
South 2	55	34	31	3	9
South 3	50	47	35	6	15
South 4	66	30	27	3	10
Total	320	226	192	26	61

Notes. Here knots with multiple lines means two lines sufficient to deduce a wavelength ratio and therefore secure grism redshift; i.e., *not* [O III] and Hβ since a set wavelength ratio was used in the fitting algorithm.

Hβ-to-[O III] line widths from 0.1 to 1 (noting that, from the 1D spectra, all [O III] line widths are qualitatively larger than the weaker, blended Hβ line widths). In these tests, we found that an average Hβ line width of ∼0.5 that of the [O III] line width gave the best quantitative statistical fits. For 67% of the spectra, in which we detect an [O III] line, the χ^2 improves when including the Hβ line in our fit. Of these, 23% of Hβ lines had S/N > 3 and were thus included in the final catalog. Here, we adopt the higher S/N cutoff ($\gtrsim$3) than for the general catalog due to the fact that the line is blended and thus inherently contaminated by the [O III] doublet, and so only the most secure Hβ lines are included. In all cases, where it was possible to include Hβ in the line fits—and where such inclusion resulted in improved fits—the Hβ line was weaker by a factor of at least 2. Utilizing this composite [O III] + Hβ fitting technique results in 90 [O III] fluxes which are statistically improved using the reduced χ^2 metric, compared to fitting the [O III] line alone. Thirty Hβ fluxes also result from this method.

4. RESULTS

In Table 1, we list the emission-line wavelengths, line IDs, fluxes, and grism redshifts for 320 lines originating from 226 star-forming knots within 192 individual galaxies found in our search for ELGs in the PEARS South Fields. Of these, 25 galaxies (12%) exhibit multiple emitting knots, and 61 knots (27.0%) have two lines (thus providing secure redshifts; see Section 3). Our sample includes 136 [O III], 83 Hα, 30 [O II], 30 Hβ, 4 C IV, 3 C III], 2 Mg II, 1 Hγ, and 1 Ne III lines (see Table 3). Of these galaxies, 17 are CDF-S X-ray sources (Giacconi et al. 2002; N. Grogin et al. 2009, in preparation). The most common lines (Hα, [O III], and [O II]) are detectable in the redshift ranges of 0–0.4, 0.1–1.1, and 0.4–1.5 respectively, given the grism bandpass. The [O III] emitters have, in general, very high equivalent widths, with a mean rest frame equivalent width $EW_{[O III],mean} = 152$ Å at a redshift of $z \sim 0.5$. The equivalent width distributions of the Hα, [O III], and [O II] lines are shown in Figure 2.

Figure 3 shows the i'_{AB}-band continuum magnitude distribution of the 192 ELGs in the PEARS South fields. The distribution peaks around $i'_{AB} = 24$ mag for both the HUDF and the PEARS South Fields 1–4, although the falloff at fainter magnitudes is more pronounced for the shallower South Fields 1–4 data. The two-dimensional method described here is optimized to find distinct emitting knots that often are present in relatively bright galaxies—for example, face-on spirals with large star-forming regions. These generally make up the bright end of the magnitude distribution shown here. The fainter tail of the magnitude distribution is comprised largely of objects from the deeper

HUDF pointing. The distribution of emission-line fluxes for all 320 emission lines, regardless of species, is shown in Figure 4. Figure 5 shows distributions for each of the three most common emission lines in our sample: Hα, [O II], and [O III]. The flux distribution for the sample peaks at ∼1.9×10^{-17} erg cm^{-2} s^{-1} for the 20 orbit/field PEARS data (four fields) and falls off at lower values due to incompleteness of the data (Figure 5). The peak is at a slightly fainter flux for the deeper PEARS HUDF at ∼1.2×10^{-17} erg cm^{-2} s^{-1}.

Given the ACS grism resolution, contamination of the dominant lines by other nearby, unresolved lines is almost certainly present. For example, the Hα line flux measurements will contain some contribution from the [N II] λλ6548, 6584 lines. The magnitude of this contamination will differ for different galaxies, as it depends on effective temperature, ionization, and metallicity. Helmboldt et al. (2004) derive an [N II] correction as a function of R-band luminosity using the Nearby Field Galaxy Sample of spiral and irregular galaxies (Jansen et al. 2000). Other grism surveys of ELGs have used global corrections by Gallego et al. (1997), which were also derived based on a local galaxy sample. Our detection method serves to produce individual galaxy knots in a wide array of morphological types (as described in Section 3), and thus a global adoption of any one [N II] contamination correction is not straightforward. Therefore, the measured Hα fluxes are likely overestimates due to this contamination but we do not adopt a global correction. The amount of contamination can range from a few percent for, e.g., blue compact dwarf galaxies, which have unusually high ionization and low metallicity, to the factors of 0.3 and 0.5 assigned by Gallego et al. (1997) and Kennicutt (1992), respectively (however, the latter being for massive, metal-rich galaxies). For the Nearby Field Galaxy Survey (Jansen et al. 2000), [N II]/Hα ranges between 0.03 and 0.5 with a mean value of 0.27. The S/N distribution of the emission-line fluxes is shown in Figure 6. The average S/N for the sample is 11.8. This increases to 12.6 when the generally weaker, blended Hβ line measurements are excluded. Our detection methods outlined above serve to produce a final sample of high-confidence detections.
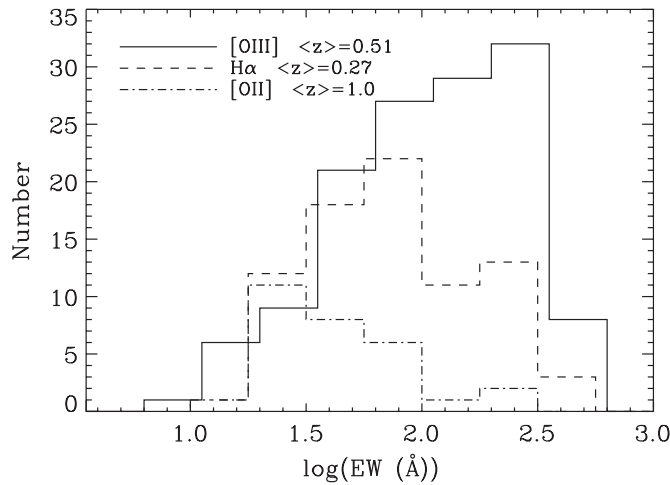
The presence of dust affects our measurements, and thus the calculations of, e.g., the SFR (Section 4.4.3) should be considered lower limits because no extinction correction was applied. The Hβ flux in principle allows an estimation of extinction for the cases in which both Hβ and Hα fall into the wavelength range of the grism and including Hβ results in a quantitatively better fit. This is only possible for a very small percentage of objects and thus we do not apply a global correction based on only these few sources. Both Hα and Hβ are measured in the spectra of objects 38750, 40816, 75753, 78582, and 123859. However, objects 40816 and 78582 are both X-ray sources and therefore likely AGN candidates (see Section 4.3). Because of this, the emission-line fluxes of these two sources are likely affected by the potential AGN component. Using only the Balmer decrement and the Milky Way or Large Magellanic Cloud (LMC) extinction law from Seaton (1979)— e.g., Calzetti et al. 1994, who find an average $E(B - V)$ of 0.4 for starburst galaxies—gives $E(B - V)$ values of 0.60, 0.26, and 0.50 for objects 38750, 75753, and 123869 (e.g., those not X-ray detected), respectively.
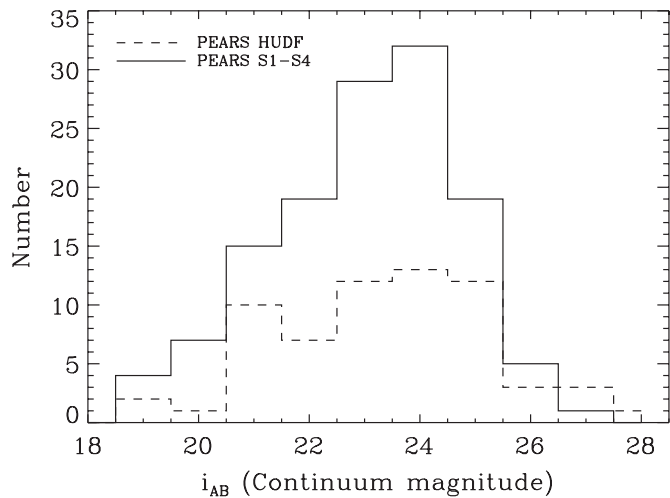
4.1. Grism Redshifts

Of the 192 ELGs, 118 have new grism spectroscopic redshifts based on our line identifications. We find eight galaxies (Table 1) that previously had no reported redshift and that have two

Table 3
Summary of Lines Detected in South Fields

Field	No. of [O III]	No. of Hα	No. of [O II]	No. of Hβ	No. of C IV	No. of C III]	No. of Mg II	No. of Ne III	No. of Hγ	No. of No ID
HUDF	43	31	13	8	1	1	1	0	0	4
South 1	20	11	6	7	1	1	0	0	0	7
South 2	26	10	4	8	1	1	1	0	0	3
South 3	22	24	4	2	0	0	0	1	1	9
South 4	26	8	4	4	0	0	0	0	0	8
Total	136	83	30	30	3	3	2	1	1	31

Figure 2. Distribution of rest-frame equivalent widths of the three most common emission lines in our sample. The median equivalent widths are 119 Å, 73 Å, and 36 Å for [O III], Hα, and [O II] respectively. The average redshifts of the three species are shown.
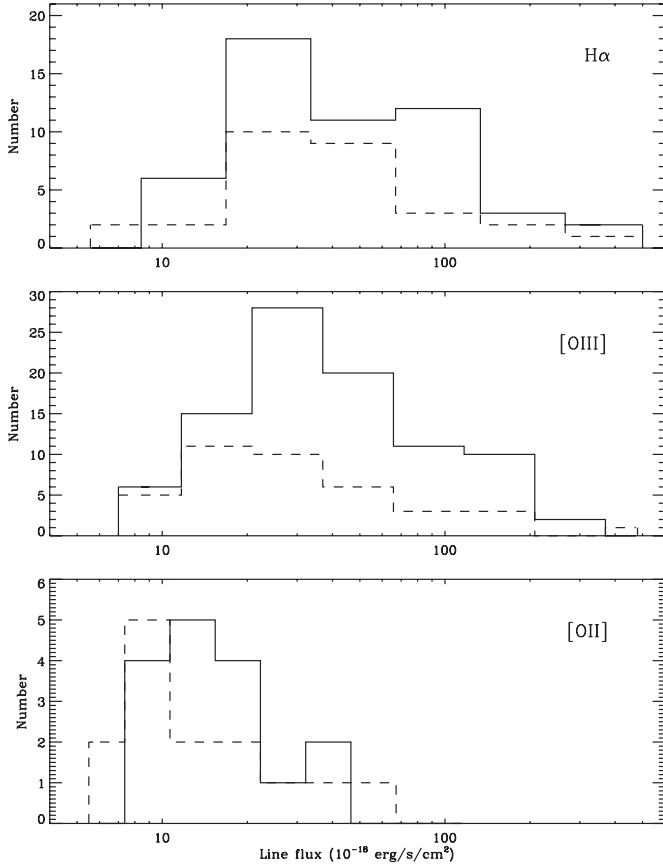

Figure 4. Distribution of ELG emission-line fluxes peaks at $\sim 2.0 \times 10^{-17}$ erg cm^{-2} s^{-1} for the PEARS South Fields 1–4 (20 *HST* orbits per field) and at $\sim 1.3 \times 10^{-17}$ erg cm^{-2} s^{-1} for the deeper (40 *HST* orbits) PEARS HUDF.

Figure 3. Distribution of ELG continuum magnitudes peaks around $i'_{AB} \sim$ 24 mag for both the HUDF and the PEARS South Fields 1–4 data. The HUDF distribution is somewhat more uniform, owing in part to a larger fraction of faint objects due to its greater depth. The clumpy face-on spirals generally make up the bright end of the magnitude distribution, while many of the HUDF sources comprise most of the faint end.

lines, allowing determination of a grism redshift from the wavelength ratios. The redshift distribution of the sample is given in Figure 7. The redshift distribution peaks at $z \sim 0.5$ and is determined by the most common emission lines within the grism bandpass: [O III], Hα, and [O II]. This explains the lower redshift peak compared to the peak in the general field galaxy

redshift distribution. The few high-redshift objects in this plot are the more rare C III], C IV, and Mg II line emitters. All of these high-redshift sources in the CDF-S are detected in the X-ray observations, and are thus likely AGN (N. Grogin et al. 2009, in preparation). The CDF-S X-ray sources are noted in Table 1.

In Figure 8, we show comparisons of our calculated grism redshifts to the available photometric and spectroscopic redshifts for the ELGs. As mentioned, for objects with only a single emission line, any previously available redshift was used to initially identify the line. This was accomplished in the cases where the line wavelength falls within the expected wavelength based on that object's previously measured redshift, within the redshift (and inherent grism) errors.

Comparison of grism-spectroscopic redshifts computed here to previously existing spectroscopic redshifts serves to demonstrate the wavelength accuracy of the grism, which is shown in Figure 8. The dispersion about the mean is 0.005 and two objects are $\gtrsim 3\sigma$ outliers: PEARS Objects 72509 and 17362, both of which are single-line detections with relatively low S/N < 3 and likely represent wavelength calibration issues. As expected, the dispersion about the mean in the photometric/grism redshifts is greater at 0.06, with the greatest $\Delta z = 0.585$ (PEARS Object 52502, the only 3σ outlier). This object has two emission lines with S/N > 5, providing a secure grism redshift based on the wavelength ratio. Object 20201, which was only marginally within 3σ of the photometric redshift also has two high S/N emission lines, as well as a clear Hβ "bump" in the [O III] line profile, further confirming its identification (Figure 9). Thus, for these two outlying objects, we are confident that the grism redshift calculated here is correct.

Figure 5. Emission-line flux distributions peak at $\sim 2.5 \times 10^{-17}$ erg cm^{-2} s^{-1}, $\sim 3.0 \times 10^{-17}$ erg cm^{-2} s^{-1}, and $\sim 1.3 \times 10^{-17}$ erg cm^{-2} s^{-1} for Hα, [O III], and [O II] respectively for the 20-orbit/field PEARS data (four fields). The PEARS HUDF line fluxes peak at slightly fainter values ($\sim 1.1 \times 10^{-17}$ erg cm^{-2} s^{-1} for [O III] and $\sim 9.0 \times 10^{-18}$ erg cm^{-2} s^{-1} for [O II]).
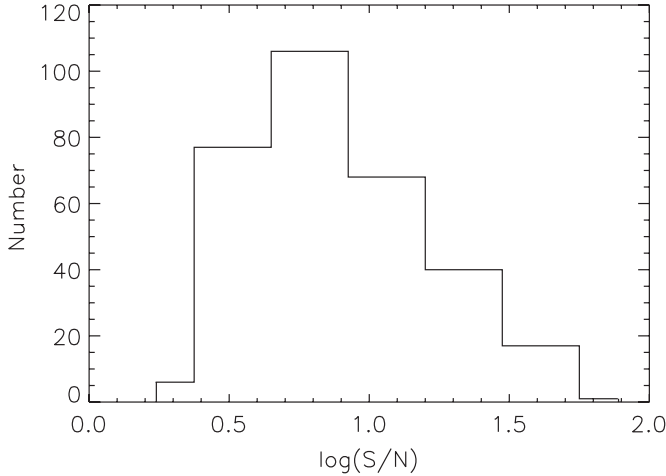
Figure 6. Distribution of signal-to-noise for all derived line fluxes. The average S/N for the sample is 11.8. This average increases to S/N = 12.3 when the weaker, blended Hβ lines are excluded. Our detection method requires a relatively high S/N because the initial grism detection images are smoothed before source extraction is performed. This is the reason we miss, e.g., lower S/N Lyα emitters (Rhoads et al. 2009).

4.2. Line Luminosities and Star formation Rates of the ELGs

Table 1 lists the line luminosities for the objects in our sample. The median Hα line luminosity is 8.3×10^{39} erg s^{-1}, and the lowest luminosity is 2.5×10^{38} erg s^{-1}. As a comparison,
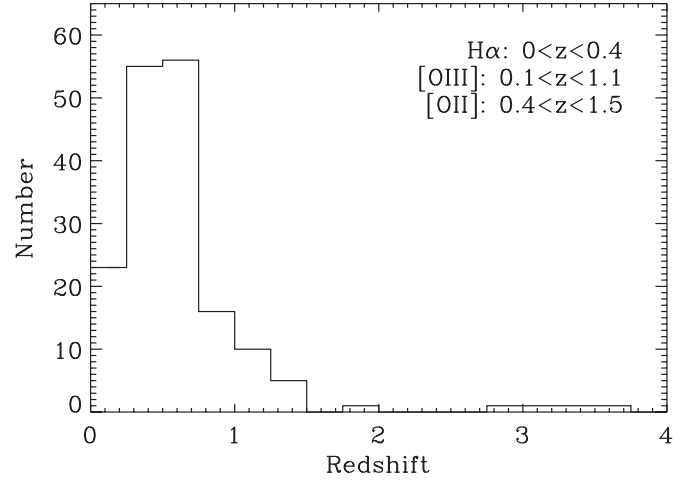

Figure 7. ELG redshift distribution. The G800L grism is sensitive from 6000–9500 Å, which yields the most common emssion lines—Hα, [O III], and [O II] in the wavelength ranges of $z = 0$–0.4, 0.1–1.1, and 0.4–1.5, respectively. The [O III] line is the most common, and thus the peak is near $z \sim 0.5$. The higher redshift objects are the more rare C III], C IV, and Mg II emitters.
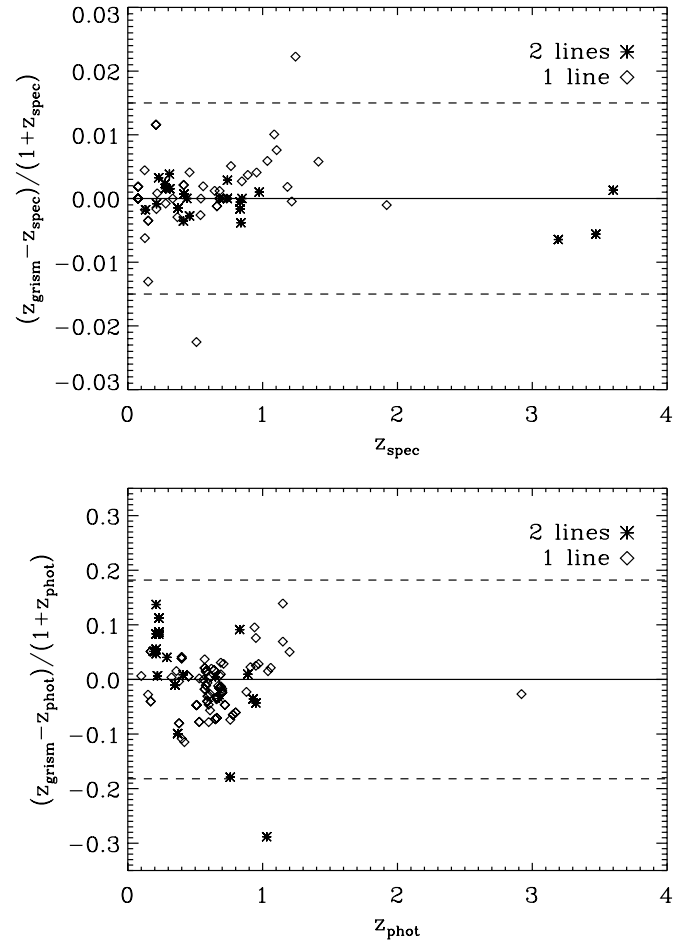
Figure 8. Comparison of available spectroscopic (top panel) and photometric (bottom panel) redshifts to the PEARS grism redshifts measured in this study, with 3σ (dashed) lines shown. 31% and 81% of PEARS-South ELGs have previously measured spectroscopic and photometric redshifts, respectively. Comparison of grism to spectroscopic redshifts essentially serves to demonstrate the wavelength/redshift calibration accuracy of the PEARS grism data. See Section 4 for a discussion on outliers.

Drozdovsky et al. (2005) find a median Hα line luminosity of 2.7×10^{40} erg s^{-1} from the ACS Grism Parallel Survey. The
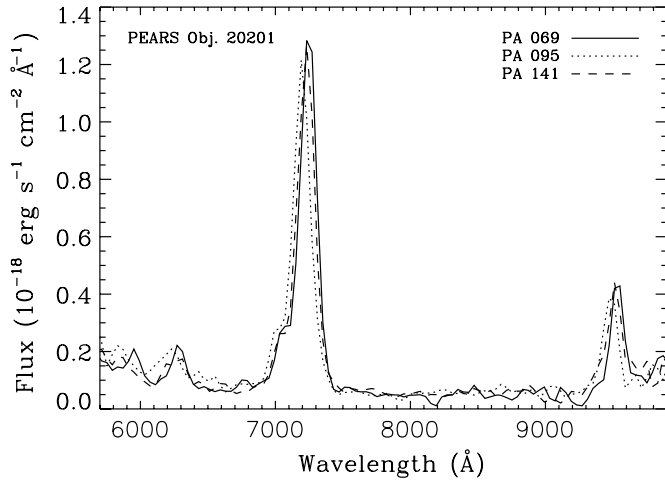
Figure 9. Example spectrum from PEARS Object 20201 at a redshift of $z = 0.445$, exhibiting the blending of Hβ and [O III]. Hα is also visible near the red end of the spectrum. An Hβ "bump" is clearly seen near 7000 Å, though not resolved from the stronger [O III] blend. In total, 31 galaxy spectra had better χ^2 fits when the Hβ line was included. Hγ and marginal Hδ are detected here, near 6300 Å and 6000 Å, respectively.

Figure 10. SFRs as a function of redshift based on the line luminosities of the ELGs. We see the expected bias of higher SFRs at higher redshifts, due to the detection limits. These SFRs are uncorrected for extinction and are thus lower limits. The approximate empirical detection limit—derived from the average limiting flux of all three lines—is shown for the (deepest) PEARS HUDF data.

typical local $L^*(\text{H}\alpha) = 7.1 \times 10^{41}$ erg s^{-1} (Gallego et al. 1995) and $L^*(\text{H}\alpha) = 3.6 \times 10^{42}$ erg s^{-1} at $z = 1.3$ (Yan et al. 1999). The median [O III] and [O II] line luminosities are 2.8×10^{40} erg s^{-1} and 6.7×10^{40} erg s^{-1}, respectively. About 96% of our emitting regions have luminosities $L \gtrsim 10^{39}$ erg s^{-1}.
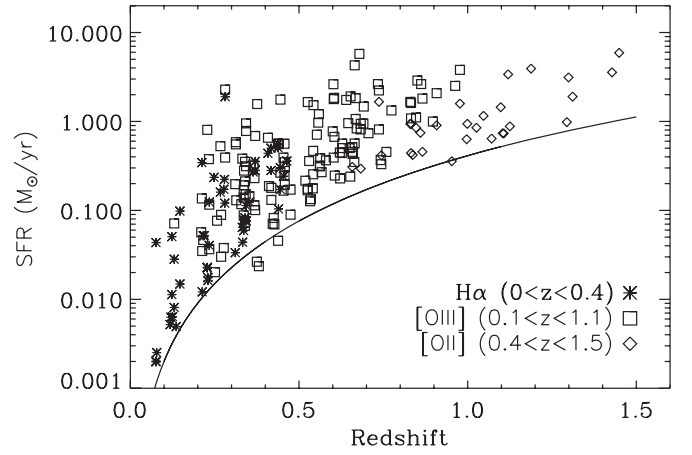
We present the SFR as a function of redshift of our ELG sample in Figure 10. SFRs are calculated using the calibrations of Kennicutt (1998) for Hα and [O II],

$$\text{SFR}_{\text{H}\alpha}\ (M_\odot\ \text{yr}^{-1}) = 7.9 \times 10^{-42}\ L(\text{H}\alpha)\ (\text{erg s}^{-1}),$$

$$\text{SFR}_{[\text{O II}]}\ (M_\odot\ \text{yr}^{-1}) = 1.4 \times 10^{-41}\ L([\text{O II}])\ (\text{erg s}^{-1}),$$

respectively for solar abundances and a Salpeter IMF for 0.1–100 $M_\odot$. The Hα luminosity is a direct measure of the ionizing output of a stellar population (under case B recombination) and thus can be related directly to the massive SFR. In particular, it probes the formation of the ionizing O stars, and thus is the most secure line in determining the SFRs. The SFR based on [O II] line luminosity is less secure, as differences in metallicity and other local environmental properties play a larger role in the oxygen lines (Kewley et al. 2001, 2004; Jansen et al. 2001). Kennicutt (1998), for example, reports a ∼30% uncertainty on the [O II] SFR calibration. However, the [O II] line is still calibrated well enough to deduce SFRs for galaxies at higher redshift (Cowie et al. 1996; Kennicutt 1992; Gallagher et al. 1989). We use the Kennicutt (1998) calibrations for the Hα and [O II] emitters in the PEARS-South ELG sample presented here.

The determination of SFRs from [O III] line luminosities is not as straightforward, since the [O III] flux depends quite strongly on metallicity and gas temperature (Kennicutt et al. 2000; Kennicutt 1992), and SFRs derived from the [O III]λ5007 line have a typical scatter of 3–4 when uncorrected for reddening (Moustakas et al. 2006). However, the [O III] line has been used to gain crude lower limits on the SFR (Maschietto et al. 2008; see also Teplitz et al. 2000 for a discussion of [O III] SFRs for LBGs). Maschietto et al. (2008) arrive at a lower limit of $\text{SFR}_{[\text{O III}](5007)}(M_\odot\ \text{yr}^{-1}) < 3.3 \times 10^{-42}L([\text{O III}])$ erg s^{-1} for their sample of 13 star-forming galaxies. With the ACS G800L grism resolution, the [O III]$\lambda\lambda$4959, 5007 doublet and Hβ are

blended, and while our fitting technique does fit the blended [O III]+ Hβ feature, some cross-contamination of the lines is likely. Many of the galaxy knots that contain [O III] emission originating from star formation (and not from AGN as described in Section 4.3) also have either Hα or [O II] lines in their spectra; so in these cases, it is clearly best to use the more direct Hα- or [O II]-deduced SFR. For the emitting regions in which only an [O III] line is detected—due to the Hα or [O II] lines falling out of the grism bandpass—we derive the [O III] SFR by using the [O III]:Hα ratio from the galaxy knots that do have both emitting lines. Since the [O III] $\lambda\lambda$4959, 5007 doublet is blended, we use $0.66 \times L_{[\text{O III}]}$ in order to estimate the contribution from the λ5007 line only. We thus arrive at

$$\text{SFR}_{[\text{O III}]}(M_\odot\ \text{yr}^{-1}) = (6.4 \pm 4.0) \times 10^{-42}\ L([\text{O III}])\ (\text{erg s}^{-1}).$$

While there is large scatter in the [O III]-derived SFR, we find no indication of nonlinearity in the relation of Hα and [O III] for this subsample of ELGs. The possible presence of residual blended Hβ flux described above provides an additional source of error to the [O III] flux derivation. However, in all cases, we did not apply extinction corrections, and thus the implied SFRs presented here are in general lower limits. In addition, we assume that most of the galaxies' active star formation is occurring in these emission-line regions, but note that the sample is incomplete in the sense that only the brightest knots of the galaxies are detected, and diffuse emission is missed in our method. Figure 10 shows the expected bias of lower SFRs at lower redshift. This in general follows calculations performed in similar studies, e.g., Drozdovsky et al. 2005, who computed SFRs of a grism-selected sample of ELGs.

4.3. Potential AGN Candidates Among the ELG Sample

Adjusting our line fitting algorithm to include Hβ fits allows us to gain a crude estimate of excitation. In Figure 11, we show the [O III]:Hβ line ratio compared to a large sample of Sloan Digital Sky Survey (SDSS) AGNs. Kauffmann et al. (2003) compare this line ratio to [N II]λ6583/Hα and thus define a region of likely AGNs (as compared to starburst galaxies) in a Baldwin, Phillips, & Terlevich (BPT) diagram (Baldwin et al. 1981; see also Kewley et al. 2001). In the grism data,
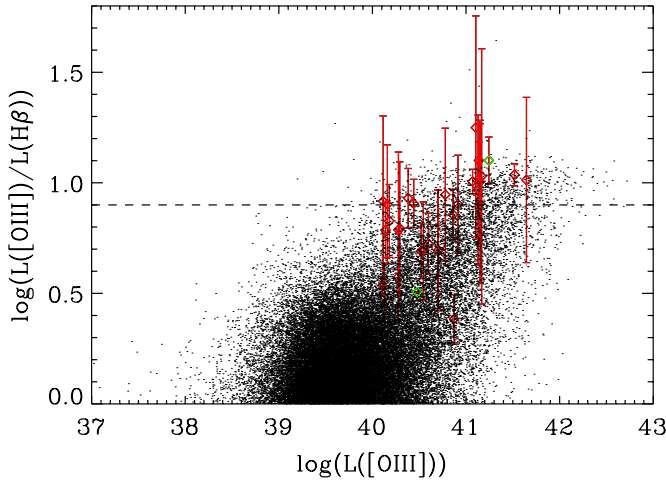
Figure 11. [O III] to Hβ flux ratios of PEARS ELGs (red diamonds) compared to those from the SDSS AGN catalog (dots; Kauffmann et al. 2003). As discussed in Section 4, the PEARS objects with [O III]:Hβ ≳ 8 (dashed line) are probable AGNs. The two green diamonds are the two X-ray confirmed objects that have both [O III] and Hβ measured (PEARS Objects 40816 and 78582).

(A color version of this figure is available in the online journal.)

the [N II] line is blended with Hα and is not possible to de-blend, as is the case with some objects for [O III] and Hβ, and thus a BPT diagram is not possible to construct from the PEARS ELGs. However, starburst galaxies with [O III]:Hβ ⩾ 8—taking into account the blending of the [O III] doublet—are extremely rare based on the starburst/AGN demarcations made by both Kauffmann et al. (2003) and Kewley et al. (2001), which include effects of metallicity and dust. We thus conclude that the PEARS objects that lie above this threshold are potential AGN candidates among our ELG sample. There are a total of 27 ELGs that have both [O III] and Hβ measured in at least one of their knots. Of these, three have $F([O III])/F(Hβ) ⩾ 8$ within their observational uncertainties, and another 14 have likely $F([O III])/F(Hβ) ⩾ 8$ but with larger errors (see Figure 11).

In addition to high [O III]:Hβ line ratios, high X-ray lumi-nosities are also strong indicators of AGN activity. Grogin et al. (2007) and N. Grogin et al. (2009, in preparation) investigate CDF X-ray sources that fall within the PEARS area. In total, 17 of the emission-line sources detected in this study overlap with the Grogin et al. PEARS X-ray sample. Of these 17, eight objects have X-ray luminosities $L_X ⩾ 10^{42}$ erg s^{-1} and are thus likely AGNs. These $L_X ⩾ 10^{42}$ erg s^{-1} sources display mainly the expected AGN lines (e.g., C III], C IV, and [Mg II]). All matches to CDF-S X-ray sources are noted in Table 1.

Of the PEARS emission-line sources with both the [O III] and Hβ lines measured, two are also X-ray sources (N. Grogin et al. 2009, in preparation), but with $L_X < 10^{42}$ erg s^{-1}. One of these two objects, PEARS Object 40816 at redshift $z = 0.281$, has a quite high flux ratio $F([O III])/F(Hβ) = 12.6$ and an X-ray luminosity of $L_X = 2.1 \times 10^{41}$ erg s^{-1}. Object 40816's line emission originates from the galaxy's nucleus. The galaxy appears to be interacting with a nearby disk galaxy (PEARS Object 35818) with a tidal stream in between the two objects. Given this PEARS Object 40816's high $F([O III])/F(Hβ)$ and moderate L_X values, one can interpret this source as being a potential obscured interaction-induced AGN. The other object, PEARS Object 78582 with redshift $z = 0.454$, has a flux ratio $F([O III])/F(Hβ) = 3.2$ and $L_X = 1.8 \times 10^{41}$ erg s^{-1}. This source appears spheroidal with signs of tidal debris and/or interaction with PEARS Object 78762. Object 78582 is thus likely a regular

star-forming galaxy with starburst-related X-ray emission, given its lower $F([O III])/F(Hβ)$ value. As Figure 11 demonstrates, the PEARS AGN candidates based on the [O III]:Hβ ratio reside mainly on the upper right locus of the SDSS sample (black dots). The lack of objects with lower excitation is likely a result of the de-blending of the [O III] and Hβ lines—as was noted in Section 3.3, the Hβ line was weaker by a factor of at least 2 in spectra where both lines were fit. We thus conclude that inclusion of Hβ in the line-fitting procedure when possible provides a way in which to select probable AGN from the grism data for follow-up study and confirmation.

4.4. High-redshift Star-forming Regions

One of the main advantages of the two-dimensional-detection method used for this study is the detection of emission lines in distinct star-forming regions within galaxies at intermediate redshift—regions that would not have been detected if the spectrum of the entire galaxy was extracted (Figure 1). In ∼12% of galaxies, we find multiple emitting knots (Figure 12). Many of these multiple-knot emitters are clumpy spirals with distinct star-forming regions. In total, 25 galaxies have multiple emitting knots. Within these galaxies, there are 59 such knots with 83 emission lines total—the majority of which are Hα. The median redshift of the subsample of multiple-emitting knot ELGs is $z = 0.336$, and the highest redshift multiple-knot emitter is at $z = 0.653$. While properties of local individual H II regions have been studied for some time (e.g., Hodge 1969; Shields 1974; Shields 1990; McCall et al. 1985; Zaritsky et al. 1994; Gordon et al. 2004; Kennicutt 1984), grism surveys such as PEARS—combined with the two-dimensional-detection method used here—are useful for finding spectra of individual intermediate-redshift star-forming regions. As discussed in Section 4.2, our detection limit serves to produce a sample of mostly *giant* star-forming regions, which have been studied extensively in the local universe since they are sites of the most extreme star formation known (e.g., Shields 1990; Giannakopoulou-Creighton et al. 1999). We find that within an individual galaxy, the Hα-derived SFR typically differs by a factor of 2 or 3 between knots. The most extreme differences in SFRs across individual galaxies do not occur in the face-on spirals that are quite common in the subsample of multiple-emitting knot galaxies, but in clumpy galaxies with clear merger signatures. This effect is not unexpected, since mergers are known to induce enhanced star formation activity which is revealed through the galaxies' emission lines. Regions of the galaxy that are undergoing more intense physical alterations due to the merging activity presumably exhibit more intense star formation.

One of the questions that can be addressed through the two-dimensional-detection technique concerns how the galaxies' giant star-forming knots are distributed radially within each galaxy. As with giant H II regions generally, these radial distri-bution studies have typically been performed on nearby spiral galaxies (Hodge 1969; Hodge & Kennicutt 1983; Athanassoula et al. 1993; Gonzalez Delgado & Perez 1997) with normal (e.g., not giant) H II regions. Since the grism data and detec-tion method used here is optimized to find the brightest star-forming regions only, a direct comparison to these studies is not straightforward. However, we examine here a subset of 10 of the multiple-knot emitters—excluding visually disturbed galaxies such as mergers and objects with nearby companions—in order to determine the radial distribution of H II regions. We exclude irregular galaxies and/or mergers—that could have emitting knots in the tidal tail, for example—since such enhanced star
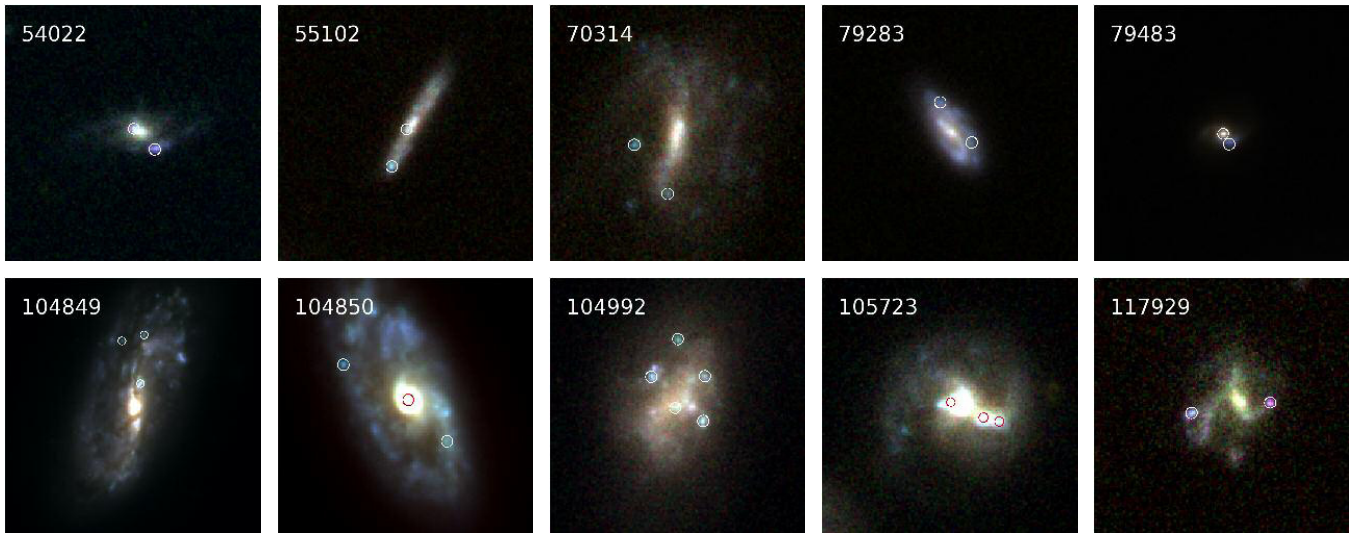
Figure 12. Subset of PEARS ELGs with multiple emitting knots as described in Section 4.3, from which the radial distribution of star-forming knots is derived. PEARS IDs are given in upper-left corners of stamps, which are 5 arcsec on a side. Circles indicate region of line emission (colored circles are for visual aid only in bright regions). The automated two-dimensional-detection method is optimized to detect line emission in galaxy knots as shown here. The radial distribution of the galaxy knots shown here is given in Figure 13. 13.

(A color version of this figure is available in the online journal.)

formation is likely induced predominantly by the dynamics of the interaction and not that which normally occurs in undisturbed disk galaxies. Such exclusion of irregular galaxies in radial distribution studies was also done by, e.g., Athanassoula et al. (1993). This subset of 10 galaxies with multiple emitting knots contains a total of 26 knots, within a redshift range of 0.076–0.483 (seven of which are above $z \gtrsim 0.1$). The galaxy knots are distributed across the faces of the galaxies as shown in Figure 12.

The distribution of PEARS galaxy knots (Figure 13) peaks around the normalized half-light radii (obtained from the GOODS catalogs). A few of these could be considered nuclear star-forming knots, as is seen in Figure 12. As a comparison to the PEARS star-forming regions at an average redshift $z = 0.242$, we also plot the radial distribution of well-studied giant extragalactic H II regions (Kennicutt 1984; Blitz et al. 1981; Castaneda et al. 1992; Rosa et al. 1984) in the local universe. This sample is drawn from M101, M33, and M51. From these relatively small samples, we see a peak in both the local and PEARS galaxies' giant star-forming regions around the half-light radius. We note here that since the median radial distance is much larger than the ACS resolution for the PEARS galaxies, the peak is not due to resolution effects. Since line emission from giant H II regions is a good tracer of massive star formation—which is a proxy to the galaxies' evolution—this result suggests that if there is a fundamental physical parameter governing the normalized radial distance at which these giant star-forming complexes form, it persists to intermediate redshifts probed in this study.

5. SUMMARY

We present results from a search for ELGs in the five PEARS South Fields, including the HUDF. We outline briefly the method used to arrive at our catalog, which relies on spectral extractions from individual emitting knots within galaxies, detected first in the two-dimensional grism image. In this way, we detect emission-line sources that would likely otherwise be missed in the standard extraction of entire galaxies, where continuum flux
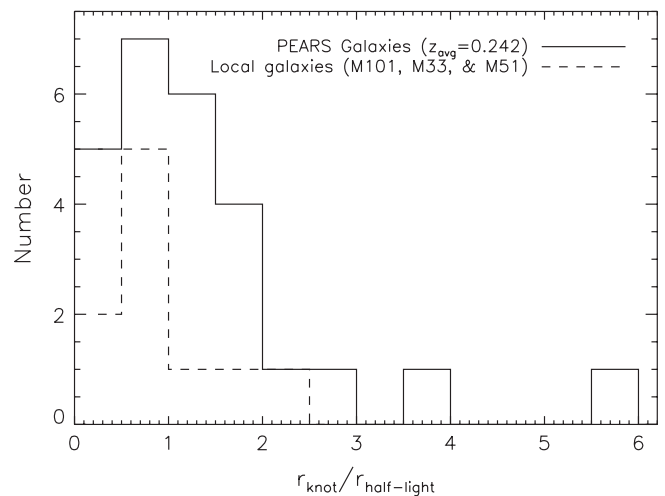
Figure 13. Comparison of radial distributions of star-forming regions within the PEARS galaxies that have multiple (giant) star-forming knots to a sample of local galaxies with well-known giant H II regions. Radial knot distances are all scaled to the half-light radii of the galaxy, as described in detail in the text. A few of the PEARS knots shown here could be considered nuclear. The PEARS sample of galaxies with multiple–emitting knots has an average redshift of $z = 0.242$, and both samples peak near the half-light radius.

can often dominate the spectrum and wash out the line. Here we summarize our findings.

1. We detect 320 emission lines from 226 galaxy knots within 192 individual galaxies. The most common emission lines are [O III], Hα , and [O II]—we detect 136, 83, and 30 emission lines of each species, respectively. We detect 25 galaxies with multiple emitting knots.

2. In Table 1, we present 118 new grism spectroscopic redshifts in the GOODS-South Field. Line identifications are obtained by either wavelength ratios where two lines are present in a given spectrum, or by utilizing previously measured—typically photometric redshifts for these objects as a first-guess.

3. We calculate SFRs of the ELG sample using Hα and [O II] where available, and derive an [O III] SFR based on the more

dependable lines when two lines are available in the spectra. The SFR as a function of redshift is given in Figure 10.

4. Including blended Hβ in our line fits results in identification of probable AGN based on approximate excitation levels. In comparison to AGN from SDSS, we find that the PEARS AGN candidates are situated in the high-excitation, high-luminosity region of the distribution.

5. The two-dimensional-detection method used for the PEARS South grism data is optimal for the detection of individual star-forming regions in galaxies up to $z \sim 0.5$. We find that the normalized radial distance of giant star-forming knots peaks near the half-light radii of the galaxies—as does a comparison sample of nearby giant H II regions in M101, M31, and M51.

Future work will begin with analysis of the PEARS North Fields data, which are currently being reduced, and will result in the second in this series of papers. Detailed studies using sources from both the PEARS South and North Fields will include an in-depth study of line luminosity functions and SFR densities, which will be possible once simulations of the data are completed in order to obtain accurate estimates of incompleteness. Future slitless spectroscopy studies with the Wide-Field Camera 3, which was installed on *HST* in Servicing Mission 4, will provide a wealth of information and confirmation for the objects already identified here, as well as detection of new ELGs at higher redshifts. Additionally, the *James Webb Space Telescope* (Gardner et al. 2006) will extend the study of ELGs to still longer wavelengths—and higher redshifts—adding vastly to our knowledge of actively star-forming galaxies which are fundamental in the overall study of galaxy evolution.

REFERENCES

Athanassoula, E., Garcia-Gomez, C., & Bosma, A. 1993, A&AS, 102, 229
Baldwin, J. A., Phillips, M. M., & Terlevich, R. 1981, PASP, 93, 5
Bertin, E., & Arnouts, S. 1996, A&AS, 117, 363
Blitz, L., Israel, F. P., Neugebauer, G., Gatley, I., Lee, T. J., & Beattie, D. H. 1981, ApJ, 249, 76
Brinchmann, J., Charlot, S., White, S. D. M., Tremonti, C., Kauffmann, G., Heckman, T., & Brinkmann, J. 2004, MNRAS, 351, 1151
Calzetti, D., Kinney, A., & Storchi-Bergmann, T. 1994, ApJ, 429, 582
Castaneda, H. O., Vilchez, J. M., & Copetti, M. V. F. 1992, A&A, 260, 370

Cohen, S. H., et al. 2009, BAAS, 41, 250
Cowie, L., Songaila, A., Hu, E. M., & Cohen, J. G. 1996, AJ, 112, 839
Drozdovsky, I., Yan, L., Chen, H., Stern, D., Kennicutt, R. C., Jr., Spinrad, H., & Dawson, S. 2005, AJ, 130, 1324
Ferreras, I., et al. 2009, ApJ, submitted (arXiv:0908.0739)
Gallagher, J. S., Hunter, D. A., & Bushouse, H. 1989, AJ, 97, 700
Gallego, J., Garcia-Dabo, C. E., Zamorano, J., Aragon-Salamanca, A., & Rego, M. 2002, ApJ, 570, L1
Gallego, J., Zamorano, J., Aragon-Salamanca, A., & Rego, M. 1995, ApJ, 455, L1
Gallego, J., Zamorano, J., Rego, M., & Vitores, A. G. 1997, ApJ, 475, 502
Gardner, J. P., et al. 1998, ApJ, 492, L99
Gardner, J. P., et al. 2006, Space Sci. Rev., 123, 485
Giacconi, R., et al. 2002, ApJS, 139, 369
Giannakopoulou-Creighton, J., Fich, M., & Wilson, C. D. 1999, ApJ, 522, 238
Glazebrook, K., Tober, J., Thomson, S., Bland-Hawthorn, J., & Abraham, R. 2004, AJ, 128, 2652
Gonzalez Delgado, R. M., & Perez, E. 1997, ApJS, 108, 199
Gordon, K. D., et al. 2004, ApJS, 154, 215
Grazian, A., et al. 2006, A&A, 449, 951
Grogin, N. A., Malhotra, S., Rhoads, J., Cohen, S., Hathi, N., Windhorst, R., & Pirzkal, N. 2007, BAAS, 211, 4605
Helmboldt, J. F., Walterbos, R. A. M., Bothun, G. D., O'Neil, K., & de Blok, W. J. G. 2004, ApJ, 613, 914
Hodge, P. W. 1969, ApJ, 155, 417
Hodge, P. W., & Kennicutt, R. C., Jr. 1983, ApJ, 267, 563
Jansen, R. A., Fabricant, D., Fran, M., & Caldwell, N. 2000, ApJS, 126, 331
Jansen, R. A., Franx, M., & Fabricant, D. 2001, ApJ, 551, 825
Kauffmann, G., et al. 2003, MNRAS, 346, 1055
Kennicutt, R. C., Jr. 1983, ApJ, 272, 54
Kennicutt, R. C., Jr. 1984, ApJ, 287, 116
Kennicutt, R. C., Jr. 1992, ApJ, 388, 310
Kennicutt, R. C., Jr. 1998, ARA&A, 36, 189
Kennicutt, R. C., Jr., Bresolin, F., French, H., & Martin, P. 2000, ApJ, 537, 589
Kewley, L. J., Dopita, M., Sutherland, R., Heisler, C., & Trevena, J. 2001, ApJ, 556, 121
Kewley, L. J., Geller, M. J., & Jansen, R. A. 2004, AJ, 127, 2002
Kurk, J. D., Pentericci, L., Rottgering, H. J. A., & Miley, G. K. 2004, A&A, 428, 793
Maschietto, F., et al. 2008, MNRAS, 389, 1223
McCall, M. L., Rybski, P. M., & Shields, G. A. 1985, ApJS, 57, 1
McCarthy, P. J., et al. 1999, ApJ, 520, 548
Meurer, G. R., et al. 2007, AJ, 134, 77
Moustakas, J., Kennicutt, R. C., Jr., & Tremonti, C. A. 2006, ApJ, 642, 775
Pirzkal, N., et al. 2004, ApJS, 154, 501
Pirzkal, N., et al. 2006, ApJ, 636, 582
Rhoads, J., et al. 2009, ApJ, 697, 942
Rosa, M., Joubert, M., & Benvenuti, P. 1984, A&AS, 57, 361
Ryan, R. E., et al. 2007, ApJ, 668, 839
Seaton, M. J. 1979, MNRAS, 187, 73
Shields, G. A. 1974, ApJ, 193, 335
Shields, G. A. 1990, ARA&A, 28, 525
Shim, H., Colbert, J., Teplitz, H., Henry, A., Malkan, M., McCarthy, P., & Yan, L. 2009, ApJ, 696, 785
Straughn, A. N., et al. 2008, AJ, 135, 1624
Teplitz, H. I., Collins, N. R., Gardner, J. P., Hill, R. S., & Rhodes, J. 2003, ApJ, 589, 704
Teplitz, H. I., et al. 2000, ApJ, 542, 18
Westra, E., & Jones, H. D. 2008, MNRAS, 383, 339
Xu, C., et al. 2007, AJ, 134, 169
Yan, L., McCarthy, P. J., Freudling, W., Teplitz, H. I., Malumuth, E. M., Weymann, R. J., & Malkan, M. A. 1999, ApJ, 519, L47
Zaritsky, D., Kennicutt, R. C., & Huchra, J. P. 1994, ApJ, 420, 87